

A simple model for arbitrary pollution effects on rotating free-surface flows

Antoine Faugaret^{1,2}, Yohann Duguet², Yann Fraigneau² and Laurent Martin Witkowski^{2,3,†}

¹Sorbonne Université, Collège Doctoral, F-75005 Paris, France

²Université Paris-Saclay, CNRS, LISN, 91400 Orsay, France

³Faculté des Sciences et Ingénierie, Sorbonne Université, UFR d'Ingénierie, F-75005 Paris, France

(Received 8 June 2021; revised 30 September 2021; accepted 28 October 2021)

In an experimental context, the contamination of an air–liquid interface by ambient pollutants can strongly affect the dynamics and the stability of a given flow. In some configurations, the interfacial flow can even be blocked by surface tension effects. A cylindrical free-surface flow driven by a slow rotating disc is considered here as a generic example of such effects and is investigated both experimentally and numerically. We suggest here a simple numerical model, without any superficial transport of the pollutants, adaptable into any code for single-phase flows. For the stationary axisymmetric base flow, the radial velocity at the interface is set to zero whereas the usual stress-free boundary conditions are retained for the perturbations. The model does not feature any free parameter. For a geometrical aspect ratio of 1/4, known to display ambiguous behaviour regarding stability thresholds, the modal selection as well as a nonlinear stability island found in the experiments are well reproduced by the model, both qualitatively and quantitatively. The robustness of the model has also been validated by replacing the radial velocity profile by a more accurate experimental fit, with very little influence on the stability results.

Key words: rotating flows

1. Introduction

Flows featuring gas–liquid interfaces abound in all areas of fluid dynamics. When the effects of impurities are neglected, the dynamics of these interfacial flows is reasonably well understood. For low enough Froude numbers, the interface is flat. While the usual no-slip condition holds near solid boundaries, for negligible gas viscosity, the dynamics at the gas–liquid interface is usually modelled using a simple stress-free condition along

† Email address for correspondence: laurent.martin_witkowski@sorbonne-universite.fr

© The Author(s), 2022. Published by Cambridge University Press. This is an Open Access article, distributed under the terms of the Creative Commons Attribution licence (<https://creativecommons.org/licenses/by/4.0/>), which permits unrestricted re-use, distribution, and reproduction in any medium, provided the original work is properly cited.

a non-deformable surface. This 'stress-free' interface condition expresses the nullity of the gradient of the tangential velocity in the direction normal to the interface, whereas a no-slip condition expresses the nullity of the velocity relative to the interface. Once the boundary conditions are well chosen, solutions to the governing equations can be sought either analytically or numerically.

This simple approach breaks down however in practice when the working fluid is standard or demineralised water, as opposed to e.g. castor oil (Batchelor 2000). The (unavoidable) presence of dust implies particles of various sizes adhere to the interface via multiple forces such as van der Waals interactions, covalent bonds, dipolar interactions and so forth. As it stands, for relatively low pollutant concentrations, a monomolecular layer of particles forms by adsorption at the interface (Scriven 1960; Bernal *et al.* 1989; Lopez & Hirsra 1998; Ponce-Torres & Vega 2016). The surface tension is locally lower where the pollutants are present, which induces a heterogeneous distribution of surface tension and hence tangential Marangoni stresses. This effect has been reported in various interfacial flows including bubbles (see e.g. Batchelor 2000 or Magnaudet & Eames 2000) and Faraday experiments (Martín & Vega 2006). It is traditionally modelled using boundary conditions that rely on a closure between the local concentration c and the surface tension σ . Such models where $\sigma = f(c)$ imply the calibration of many constants, some of them possibly time-dependent (Ponce-Torres & Vega 2016), whereas the real chemical composition and even the concentration of the pollutants are rarely known in detail. A really simple phenomenological model is therefore called for to address most polluted interfaces at once, irrespective of their exact composition and properties. The goal of this paper, by considering a simple enough flow prototype, is to introduce and validate such a phenomenological model by comparing its numerical prediction to experimental results.

In this work, the free-surface flow spinning above a rotating disc is considered at low rotation rates. The cylindrical sidewall is held at rest. This flow is characterised geometrically by the aspect ratio $G = H/R$, where H is the undisturbed fluid height and R the interior radius, and dynamically by a Reynolds number $Re = \rho\Omega R^2/\mu$ based on the rotation rate Ω , the liquid density ρ and the dynamic viscosity μ (Hyun 1985; Spohn & Daube 1991; Spohn, Mory & Hopfinger 1993; Lopez 1995; Iwatsu 2004, 2005; Piva & Meiburg 2005; Bouffanais & Lo Jacono 2009; Cogan, Ryan & Sheard 2011). The comparison performed by Spohn & Daube (1991) between experimental and computational velocity profiles obtained using the free-slip boundary condition has revealed that for $G = 7/4$, there is a mismatch in the tangential velocity profiles especially near the liquid–air interface. The value of G that caught our attention is $G = 1/4$. In this geometry, a mode $m = 3$ (where m is the dominant azimuthal wavenumber) was identified experimentally as the first instability encountered when increasing Re (Miraghaie, Lopez & Hirsra 2003; Lopez *et al.* 2004). Numerical simulations were also reported in the same papers and summarised recently by Hirsra & Lopez (2021). A mode $m = 3$ was also reported in this study as the most unstable mode. The numerical domain used consisted however of two mirror-concatenated copies of the original domain, which has the unphysical property of allowing for mass transfer through the mid-plane representing the interface. To our knowledge, no simulation of the original geometry has been reported using stress-free boundary conditions until the recent study of Faugaret (2020). In that study, linear stability analysis based on the stress-free boundary condition leads to a modal selection at odds with the experimental results reported earlier: the first unstable mode occurs at higher Re than in the experiment and has the symmetry $m = 2$ rather than $m = 3$. Thus $G = 1/4$ appears particularly demanding from a bifurcation point of view and represents an interesting test for a modelling strategy.

The first investigations to blame the presence of surfactant-like pollutants for the observed mismatch were performed by Spohn & Daube (1991), as well as Lopez, Hirta and co-authors (Lopez & Chen 1998; Lopez & Hirta 1998). A numerical investigation of the same system with $G = 1/4$ was conducted by Kwan, Park & Shen (2010) by assuming a finite concentration of a given surfactant at the interface rather than using a stress-free boundary condition. A parabolic closure was used to link the surface tension to the superficial concentration field. This work is useful as a confirmation of the modal instability observed in experiments, yet it does not contain any parametric study nor any bifurcation diagram. In general, the stability threshold values found in experiments match those predicted in numerics using free-slip conditions, provided the aspect ratio G is large enough, as in the case where $G = 2$ (Lopez *et al.* 2004; Serre & Bontoux 2007; Cogan *et al.* 2011; Faugaret 2020). The situation is entirely different for values of G below unity. In a recent publication, Faugaret *et al.* (2020) carried out a joint experimental/numerical study of the same flow for a smaller aspect ratio $G = 1/14$. This aspect ratio is characterised by a much greater mismatch between thresholds in Re (Poncet & Chauve 2007; Kahouadji, Martin Witkowski & Le Quéré 2010). A simple surfactant-free model, initially suggested by Spohn & Daube (1991), was found to lower significantly the stability threshold Re_c without fully resolving the mismatch. In this model, the radial velocity u_r is assumed to be zero over the entire interface, whereas the azimuthal component only has zero normal derivative. This approximation is known in other (often two-dimensional) flow conditions as the ‘stagnant cap approximation’. We do not use this denomination to emphasize that the condition holds here on the radial component only. At the very end of the paper by Faugaret *et al.* (2020), a ‘mixed model’, intermediate between the stress-free and the Spohn–Daube model, was suggested. It was analysed using linear stability theory only. The values of Re_c associated with this model are quantitatively much closer to the experimental thresholds. This suggests a deeper analysis of the model using a fully nonlinear methodology. The goal of the present investigation is first to justify the model based on a new experimental campaign, then assess its ability to reproduce the experimental dynamics qualitatively and quantitatively. The present study relies on an experimental set-up, a linear stability solver and a direct numerical simulation code with the mixed boundary condition implemented. This new study departs from the former numerical investigation of Faugaret (2020) and Faugaret *et al.* (2020) by the use of fully nonlinear simulations as well as the different physics associated with another value of G .

The plan of the paper is as follows: § 2 contains a description of the tools used in the whole study. In § 3, the validity of the stress-free boundary conditions is questioned in light of a new Lagrangian tracking experiment. The model is introduced both in stationary and non-stationary flow conditions. The joint experimental/computational analysis of the bifurcations resulting from the modified base flow is reported in § 4 before the conclusions in § 5. The numerical methods and their validation are explained in the [Appendices A and B](#), while [Appendix C](#) details both experimental and numerical protocols followed to highlight the hysteresis.

2. Experimental set-up and numerical tools

2.1. Experimental set-up

The experimental set-up is sketched in [figure 1](#). It consisted of a cylindrical Plexiglas cavity with an internal radius of $R = 140.3 \pm 0.05$ mm. The cavity was closed at its bottom to prevent any leak. A disc of radius $R_d = 139.6$ mm was mounted inside the cavity. The gap between the disc and the cavity was filled with liquid. The angular

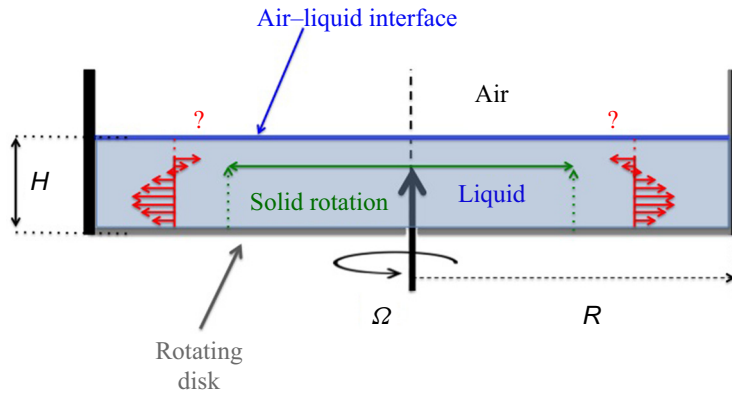


Figure 1. Sketch of the flow over a rotating disc with fixed cylindrical sidewall, with geometrical parameters indicated. The exact boundary condition at the air–liquid interface in the presence of a polluted interface is being questioned.

rotation Ω of the disc was accurately controlled using a closed-loop tachometer. The liquids used in this experimental investigation were tap water, demineralised water and a water–glycerol mixture with 60 % glycerol in terms of mass. Their temperature was not controlled but was known with an accuracy of 0.1 K. The corresponding kinematic viscosity was then evaluated using an empirical formula (Cheng 2008). Overall, the experimental Reynolds number was known with an accuracy of the order of a percent for the parameters investigated.

Pointwise velocity measurements were made using a one-component laser Doppler velocimetry (LDV) device composed of a Dantec laser linked to a BSAFlow processor. The liquid was seeded with Dantec 10 μm diameter silver-coated hollow glass spheres. Optical deviation problems were fixed *a posteriori* using the method described by Huisman, van Gils & Sun (2012). The standard deviation (u_z^{rms}) of the instantaneous axial velocity component was monitored at the location ($r = 0.74 \pm 0.01$, $z = 0.5G$), at an azimuthal position fixed in the laboratory frame. The choice of the axial component was dictated by the ease of optical access. As for visualisations, non-axisymmetric flow patterns were highlighted by injecting ink into the fluid. When a glycerol mixture was used as a working fluid, ink of lighter density did not sink and stayed at the interface. The syringe used to inject ink was carefully hung with the needle barely touching the fluid interface to avoid disturbing the flow. A 26G (0.26–0.464 mm) inside–outside diameter needle proved to be a good compromise for being small enough while injecting sufficient ink flow to be visible.

Lagrangian tracking of a small particle at the interface was also performed with the 60 % glycerol mixture. The tracer in question was either ink (as mentioned above) or a solid tracer consisting of a small portion (less than 1 mm in diameter) from the outer protective sheath of an electric cable. In the latter case, the sheath could accommodate an air bubble, which together with capillary effects ensured that it stayed at the liquid interface. The respective trajectories of the ink and the tracer were monitored by filming at 30 f.p.s. using an IDS UI 3370 CP camera (2048 \times 2048 pixels) mounted above the liquid. Even though each of them was intrusive, the use of two different measurement techniques allowed us to cross-check and validate both trajectory and velocity. In particular, the good match

indicated that, despite the non-negligible size of the particle, its superficial trajectory could be considered in a first approximation as non-inertial.

Whatever the liquid mixture used, no instability was detected below $Re = 1500$. Above this value, the experimental protocol was to increase Re in steps by adjusting the rotation speed. Several step values were investigated: 1/3, 1/2, 1 or 2 r.p.m.. Each step was then observed and analysed over a time ranging from 20 to 90 min, which corresponded to at least 35 disc revolutions for water and 62 disc revolutions for the 60 % glycerol mixture. To improve the experimental reproducibility, the mixed up solution was stored for 1 to 3 days inside the vessel, with a cover plate on top to reduce contact between the air and the interface.

2.2. Numerical tools

In all numerical approaches deployed here, only the liquid phase was simulated in the non-deformable cylindrical domain $\{(r, \theta, z) \in (0 : 1) \times (0 : 2\pi) \times (0 : G)\}$. The height-to-radius ratio G was fixed to 1/4. After non-dimensionalisation by the angular velocity Ω , the radius R , the liquid density ρ and the dynamic viscosity μ , the incompressible Navier–Stokes equations in the bulk of the flow can be written as

$$\nabla \cdot \mathbf{u} = 0, \tag{2.1}$$

$$\frac{\partial \mathbf{u}}{\partial t} + (\mathbf{u} \cdot \nabla) \mathbf{u} = -\nabla p + \frac{1}{Re} \nabla^2 \mathbf{u}, \tag{2.2}$$

where $Re = \rho \Omega R^2 / \mu$. The boundary conditions which are not discussed in this work concern the sidewall ($r = 1$) and the rotating bottom ($z = 0$), both characterised by no-slip. By contrast, we have not yet specified the boundary conditions used at the liquid–gas interface located at $z = G$. The several codes described below can deal with the classical types of boundary conditions such as Neumann, Dirichlet or Robin. A given rotational symmetry \mathcal{R}_m , characterised by a fundamental azimuthal wavenumber $m > 0$, can be imposed such that the velocity field verifies

$$(\mathcal{R}_m \mathbf{u})(r, \theta, z) = \mathbf{u} \left(r, \theta + \frac{2\pi}{m}, z \right) = \mathbf{u}(r, \theta, z). \tag{2.3}$$

Steady states are defined by $\partial_t \mathbf{u} = \mathbf{0}$ in (2.2). They were identified numerically using a Newton solver. The spatial discretisation in this solver is based on a Cartesian finite difference representation in primitive variables using the exact same boundary conditions as above. The code has been validated against the formulation used by Kahouadji (2011). It yields a numerical estimation of the base flow whose associated velocity field can be written (U_r, U_θ, U_z) and depends on r and z only. The stability analysis of the base flow was carried out using an Arnoldi algorithm described in Appendix B.

As for the unsteady nonlinear simulations, we used the direct numerical simulation (DNS) code Sunfluidh developed for incompressible flows, described in Appendix A. It is based on a projection method to ensure a divergence-free velocity field. The governing (2.1) and (2.2) were discretised on a staggered structured non-uniform grid using a finite volume scheme with a second-order centred formulation in space. A second-order Backward Euler Differentiation was used for time discretisation. The nonlinear simulations were conducted without any azimuthal symmetry imposed.

The grid consisted of $160 \times 180 \times 160$ cells in r, θ and z , respectively. The timestep was set to $\Delta t = 4 \times 10^{-3}$ in units of Ω^{-1} . In the radial direction, the grid cell size varied from

8×10^{-3} at $r = 0$ to 1.2×10^{-3} at $r = 1$, and from 6×10^{-4} at $z = 0$ to 8×10^{-4} at $z = G$ with a maximum of 10^{-3} in the axial direction. The mesh was thus more refined near the periphery $r = 1$, close to the rotating disc as well as near the interface. The discretisation was uniform in the azimuthal direction.

3. Are free-slip boundary conditions appropriate?

3.1. Statement of the problem

As mentioned in § 1, determining an exact or at least effective boundary condition at the liquid–gas interface is the main goal of this study. Although a derivation from first principles is possible, it would invariably clash with the indetermination of the actual experimental conditions. We adopt here first a purely phenomenological approach that focuses on consequences rather than causes: instead of deriving the boundary conditions analytically by assessing the underlying physical mechanisms at play, we choose to simply gather experimental evidence as to how these interfacial conditions can be approximated in practice. Importantly, we begin by considering the steady regime. This regime is encountered experimentally for $Re = 3300$, the value at which these Lagrangian experiments are reported.

3.2. A Lagrangian tracking experiment

The main idea behind the present Lagrangian tracking is to quantify one of the macroscopic consequences of the interfacial boundary conditions, namely the radial drift of non-inertial tracers. Two different experimental tracking techniques have been used, one using ink and the other with a solid tracer (the sheath from an electric cable described earlier). The respective trajectories of the ink and the tracer are displayed in a sequences of superimposed images in figure 2. The trajectories of the ink and the sheath are quantitatively similar after almost two revolutions of the bottom disc. This good match ensures that both tracers, despite their differences in relative weight and the fact that one diffuses while the other does not, behave almost as neutral fluid tracers and remain at the interface. These experimental trajectories are compared with the numerical trajectories predicted for a given set of boundary conditions. Because the dynamics is steady, these numerical trajectories are evaluated by first determining the base flow $\mathbf{U} = (U_r, U_\theta, U_z)$ corresponding to the boundary conditions imposed, using the Newton solver mentioned earlier. The trajectories are later integrated numerically from solving the two-dimensional autonomous equation $(\dot{r}_p, \dot{\theta}_p) = (U_r, U_\theta/r_p)$, where (r_p, θ_p) denotes the position of the particle in the interface plane $z = G$. In particular, the numerical trajectory corresponding to the free-slip conditions $\partial_z U_r = 0$ and $\partial_z U_\theta = 0$ is shown in red in figure 2. This trajectory circles inward until it saturates at a fixed radial location, at approximately $r = R/2$. By contrast, the ink and the sheath trajectories (departing from the same initial radius located near the periphery of the flow) also spiral in but they experience a much shorter radial drift, approximately one tenth of a radius in one revolution. The fourth trajectory displayed in figure 2 in green (labelled ‘ $U_r = 0$ ’) corresponds to the trivial integration, over the same duration, of a tracer without any radial drift, i.e. with $U_r = 0$ and $\partial_z U_\theta = 0$ for all r . This last case corresponds also to the model of Spohn & Daube (1991). One of the visual conclusions from figure 2 is that the small radial drift of the two experimental trajectories (ink and sheath) is much closer quantitatively to the vanishing radial drift of the new model than to the large radial drift of the stress-free model.

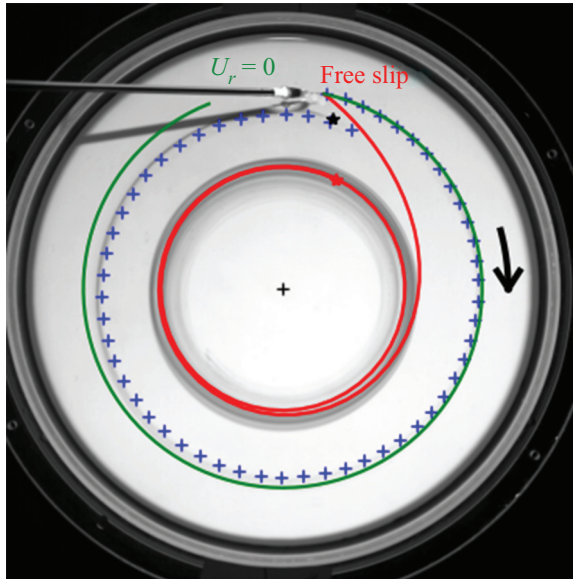


Figure 2. Lagrangian tracking experiment. Comparison between model and free-slip boundary condition, ink injection and particle tracking for $Re = 3300$, and trajectories predicted by the numerical integration of the tracer position for the stress-free model ($\partial_z U_r = 0$, red) and the new model ($U_r = 0$, green). The liquid in the experiment is a 60 % glycerol mixture. Photograph taken after the disc has achieved 1.94 revolutions after ink injection.

The radial drift of the tracer makes it move along the planar interface. The tracer hence visits the whole range of radius values from the periphery to the central zone. Both radial and azimuthal position are monitored at every time. Given that the base flow is axisymmetric and steady, the respective radial and azimuthal Eulerian velocity profiles can easily be reconstructed using finite differences. They are respectively shown in figures 3(a) and 3(b). The velocity profiles predicted for the base flow by either free-slip (red solid line) or the present model (green solid line) have been added to the figure for comparison. Compared with figure 2, figure 3(a) has the advantage of displaying the entire r -profile. As indicated by the two velocity components, the flow is in solid body rotation for $r < 0.4$ in the models, whatever the boundary condition at the interface.

The comparison of azimuthal velocity profiles $U_\theta(r)$ in figure 3(b) shows a flawless match between the experimental profile and the prediction by the new model. The free-slip profile displays, in turn, a neat excess of azimuthal velocity in the interval $0.4 < r < 0.6$ not compatible with the measurements. As for the radial component, for the free-slip boundary condition, it departs from zero and reaches negative values down to -0.17 over the range $0.6 < r < 0.8$. This is to be compared with the radial tracer velocity measured experimentally, which departs from zero only for $r > 0.6$ and does not exceed 0.03 in magnitude. The experimental radial velocity profile is hence reasonably well approximated by $U_r = 0$ for all $0 < r < 1$, rather than by the free-slip profile. This highlights again the limited relevance of the free-slip boundary condition in the steady regime.

The tracer has a finite size and cannot legitimately be considered non-inertial, which suggests that the tracer drift velocity is not exactly the radial velocity of the fluid. As a verification, the tracer is also tracked in a range of radii $[0.14-0.2]$, where the velocity field obeys solid body rotation (see figure 3b). The order of magnitude of the radial drift velocity of the tracer in this region is a measure of the inertial effects (here only owing to

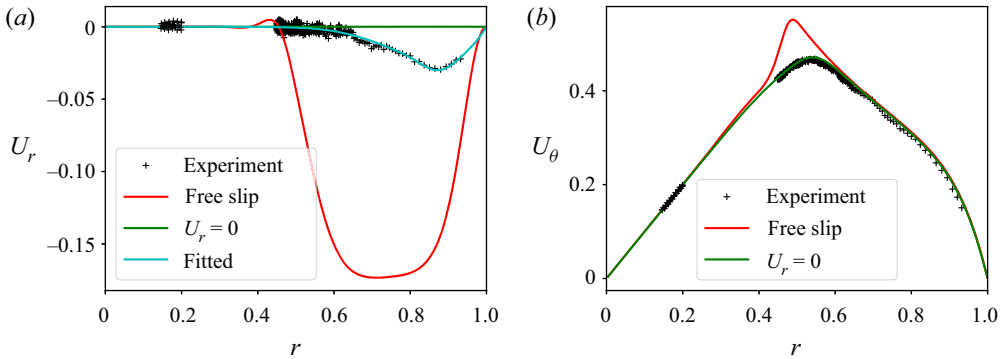


Figure 3. Same conditions and parameters as in figure 2. Velocity profiles $U_r(r)$ (a) and $U_\theta(r)$ (b) at the interface $z = G$. The cyan solid line for the radial velocity profile is a fit of the experimental data using cubic spline functions.

centrifugal acceleration). The mean value of the tracer drift velocity is 8.3×10^{-4} , which is barely visible on the scale of figure 3(a). It indicates that inertial effects have a weak influence on the radial fluid velocity measurements.

The Dirichlet condition $U_r = 0$ is only an approximation, and it is a relatively strong hypothesis. To better judge the quality of this approximation, an alternative radial velocity profile is suggested as a boundary condition. This new data-driven profile is obtained in figure 3(a) by simply fitting (rather than approximating) the experimental radial profile of U_r for $Re = 3300$ using cubic spline functions. The new profile $U_r^{exp}(r)$, compared with its experimental counterpart, displays the same variations yet in a smoother way. It can later be imposed directly in the numerical codes as another Dirichlet boundary condition $u_r(z = G) = U_r^{exp}(r)$. As a rough model allowed only in the frame of a robustness test, the same radial velocity profile is imposed independently of the value of Re .

3.3. Model boundary conditions for the steady base flow

The reasons why the usual free-slip boundary condition does not apply to the current set-up have been discussed by Lopez & Chen (1998), Faugaret *et al.* (2020) and Faugaret (2020). It is important to recall that the free-slip condition itself comes from an approximation of the force balance between the liquid and the gas at the interface. As the viscosity and surface tension of the gas phase are often neglected, the interfacial force balance reduces to the steady balance between viscous stresses and Marangoni forces in the liquid at every point of the interface.

Starting from the Boussinesq–Scriven surface fluid model for a Newtonian fluid–gas interface (Scriven 1960), assuming that the interface remains flat at all times, and under the hypothesis of negligible surface dilatational viscosity and surface shear viscosity (Hirsa, Lopez & Miraghaie 2001), the force balance leads to the following boundary conditions:

$$\frac{\partial u_r}{\partial z} = \frac{1}{Ca} \frac{\partial \bar{\sigma}}{\partial r}, \quad \frac{\partial u_\theta}{\partial z} = \frac{1}{Ca} \frac{1}{r} \frac{\partial \bar{\sigma}}{\partial \theta}, \quad u_z = 0, \quad (3.1a-c)$$

where $\bar{\sigma} = \sigma/\sigma_0$, with σ the surface tension of the liquid and σ_0 the reference surface tension. The capillary number is defined as $Ca = \mu\Omega R/\sigma_0$, with μ the dynamic viscosity. A closure $\sigma = f(c)$ for the surface tension σ is necessary, here as a function of the concentration $c = c(r)$ only. The important physical property to capture in the closure is the decrease of σ with increasing concentration, while the concentration $c(r)$ is governed

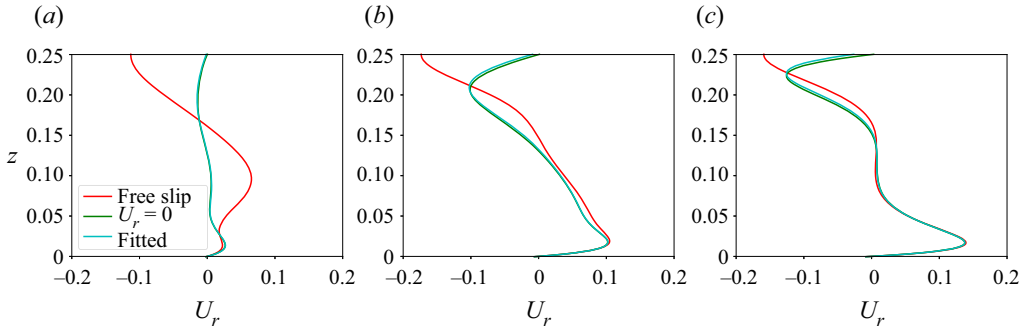


Figure 4. Radial velocity profiles at $r = 0.55$ (a), 0.70 (b), 0.85 (c) for the base flow at $Re = 3300$. Boundary conditions: free-slip (red); $U_r = 0$ (green); radial profile fitted from experiments at the same value of Re (cyan).

by in-plane advection and diffusion only (Stone 1990; Kwan *et al.* 2010). It is also assumed that surfactants remain at the interface at all times and that they neither sink towards the bulk nor undergo desorption. This is justified for low enough pollutant concentrations in the steady regime (Bandi *et al.* 2017). The effective radial velocity profile resulting from this interplay is not trivial. Faugaret *et al.* (2020) have demonstrated for the base flow for another value of G , in the limit of large concentrations, the radial profile evolves non-uniformly towards $U_r = 0$. We assume that the same result also holds here for $G = 1/4$. As for the azimuthal velocity profile, (3.1b) together with axisymmetry yields $\partial_z U_\theta = 0$, like in the free-slip boundary conditions. This is perfectly consistent with the findings of Miraghaie *et al.* (2003) in a related geometry. The impermeability condition yields $U_z = 0$.

The suggested synthetic boundary conditions for the base flow hence write:

$$U_r = 0, \quad \frac{\partial U_\theta}{\partial z} = 0, \quad U_z = 0. \quad (3.2a-c)$$

3.4. Comparison of stationary velocity profiles

The steady base flow with either the free-slip, the new model or the fitted boundary condition has been computed for $Re = 3300$ using the Newton solver. The corresponding z -profiles for the radial component are shown in figure 4 for increasing values of r , i.e. from the axis towards the sidewall. For all values of r , the three profiles match very well from $z = 0$ up to a given value dependent on r . Above this value of z , the free-slip profile deviates significantly from the two other base flow profiles. This r -dependent match is consistent with the radial development of the Ekman-like boundary layer on the rotating plate. Remarkably, the volumetric profile resulting from the fitted condition $U_r = U_r^{exp}$ differs very little from the one induced by $U_r = 0$, except very close to the interface.

A qualitative comparison of the global distribution of U_r in the meridian plane is possible at that stage. The recirculation in the meridian (r, z) plane is known to be caused by the axial gradients of u_θ . These gradients primarily arise from the lack of azimuthal entrainment at the interface, so that the flow entrained by the rotating disc is slowed down by the friction at the sidewall. The recirculating meridian flow invariably takes, near the rotating bottom wall at $z = 0$, the form of a radial flow outwards. Continuity imposes the flow to loop and recirculate inwards near the upper interface at $z = G$, with the exact profile in the upper half depending on whether free-slip or no-slip is imposed.

3.5. Unsteady regime

It is known from former investigations that for Re large enough, the axisymmetric base flow loses its stability. The resulting instability patterns are characterised by an integer m , the leading azimuthal wavenumber selected by the instability. Structurally, the corresponding modes display at saturation exactly m off-centred co-rotating vortices. These vortices are clearly visible from above using ink in the experimental figures 5(a), 5(c), 5(d) and 5(f). The approximately circular ink trajectories in the off-centred vortices are *a priori* incompatible with the condition $U_r = 0$, because vortices need a genuinely two-dimensional velocity field (note however that axial vorticity at the interface is not excluded because ω_z also contains, by definition, radial derivatives of u_θ). As a consequence, the frozen model suggested by Spohn & Daube (1991) becomes ill-adapted to unsteady simulations for which it requires a non-trivial generalisation.

New boundary conditions were suggested in the last part of the paper by Faugaret *et al.* (2020) and used only in the context of linear stability analysis. This model assumes a decomposition of the velocity field $\mathbf{u} = \mathbf{U} + \mathbf{u}'$ into an axisymmetric part \mathbf{U} with $\partial_\theta \mathbf{U} = 0$ and a residual perturbation \mathbf{u}' . Faugaret *et al.* (2020) explicitly chose \mathbf{U}_b as the base flow solution of the steady (2.1) and (2.2) (with $\partial_t = 0$) and computed with the boundary condition $U_r = 0$ at $z = G$. Such a solution is found either using the Newton method or by timestepping the unsteady equations under an axisymmetry assumption, because no axisymmetric instability occurs for the range of Re investigated. The perturbation remains subject to the classical stress-free boundary condition $\partial_z u'_r = 0$. This is different from the approach adopted by Miraghaie *et al.* (2003), where the doubt about the stress-free boundary conditions is on the perturbations rather than on the base flow like in the present model.

In the present study, we also perform unsteady nonlinear simulations based on a pre-existing well-tested numerical code. For this purpose, another decomposition $\mathbf{u} = \bar{\mathbf{U}} + \tilde{\mathbf{u}}$ into mean flow $\bar{\mathbf{U}}$ and fluctuation $\tilde{\mathbf{u}}$ is preferred for its computational simplicity. The mean flow $\mathbf{U}(r, z, t)$ is defined as the instantaneous azimuthal average

$$\bar{\mathbf{U}}(r, z, t) = \frac{1}{2\pi} \int_0^{2\pi} \mathbf{u}(r, \theta, z, t) d\theta. \quad (3.3)$$

In practice, this average needs only be performed at the interface $z = G$. Mean flow and base flow do not strictly coincide except in the linearised regime around the steady axisymmetric solution \mathbf{U}_b , where the velocity field can be written $\mathbf{u}(r, \theta, z, t) = \mathbf{U}_b(r, z) + \varepsilon \tilde{\mathbf{u}}(r, z, \theta, t) + O(\varepsilon^2)$. At order $O(\varepsilon)$, because nonlinear interactions of the perturbations to the base flow are neglected, $\bar{\mathbf{U}} \approx \mathbf{U}_b$ because $\langle \tilde{\mathbf{u}} \rangle = 0$.

The suggested synthetic boundary conditions for the mean flow in the linear regime can be written, as for the base flow, by

$$\bar{U}_r = 0, \quad \frac{\partial \bar{U}_\theta}{\partial z} = 0, \quad \bar{U}_z = 0. \quad (3.4a-c)$$

The fluctuating velocity field $\tilde{\mathbf{u}}(r, \theta, t)$ is however subject to the regular stress-free boundary conditions

$$\frac{\partial \tilde{u}_r}{\partial z} = 0, \quad \frac{\partial \tilde{u}_\theta}{\partial z} = 0, \quad \tilde{u}_z = 0. \quad (3.5a-c)$$

This full model amounts to neglecting the effect of the surfactants on the fluctuations while it is fully taken into account for the mean part.

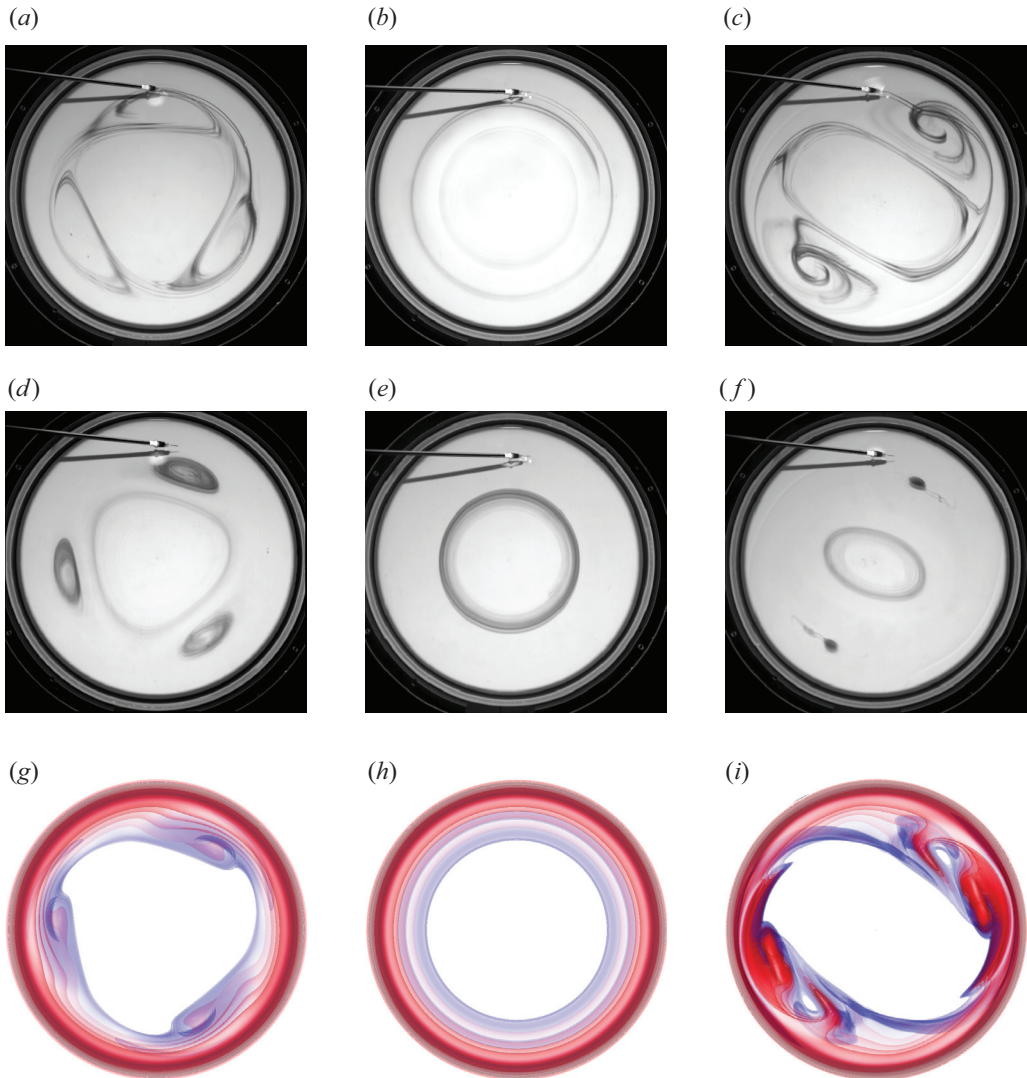


Figure 5. Instability observed for $Re = 2100$ (*a, d, g*), $Re = 3300$ (*b, e, h*) and $Re = 5545$ (*c, f, i*). (*a, b, c*) 60 % glycerol experiment, short time after ink injection. (*d, e, f*) Same experiment, long time after ink injection. (*g, h, i*) Top view of three-dimensional axial vorticity isosurfaces. The four blue and the four red isosurfaces are linearly spaced in $[-0.016, -0.04]$ and $[0.1, 0.4]$, respectively.

4. Bifurcations

In this section, we present a joint experimental/numerical investigation of the onset of unsteadiness. The numerical approach is based on the model suggested in § 3.5 and detailed in [Appendices A](#) and [B](#).

4.1. Modal selection in experiments

We begin by explaining the modal selection as observed in the experimental campaign. The protocol was carefully designed with measurements as Re is increased in small steps. We report here first only stable states that can be observed on long enough timescales

from 1 to 3–4 days after the preparation of the solution. As Re is increased from rest, the first instability is well identified. It corresponds to the instability of a mode with $m = 3$. Its onset in Reynolds number $Re_c^{(m=3)}$ depends on the experimental details such as the amount of glycerol in the solution: for a glycerol amount of 60 %, $Re_c^{(m=3)} \approx 1550 \pm 50$, while for no glycerol it lies in the range 1600–1700. This is to be compared with the value of $Re \approx 2000$ at which the instability was reported experimentally by Lopez *et al.* (2004) and Vogel *et al.* (2004). The same instability was also identified numerically by Kwan *et al.* (2010) using a quadratic surfactant model, although some parameters (which need to be calibrated) have no equivalent in our study.

The exact threshold value turns out to be very sensitive to the experimental conditions. The mode $m = 3$ is observed visually and attested in the LDV time series up to a second critical value of $Re \approx 2500$ for glycerol and 3100 for water. Above this threshold, the axisymmetric base flow is recovered over a finite range of values of Re called a stability island. Above a second onset value $Re_c^{(m=2)}$, the base flow is again unstable, yet to a mode with symmetry $m = 2$. This onset value varies within the Re -interval 3800–4800, and depends on the direction in which Re is varied. This is a clear signature of hysteresis that will be tackled later. Measurements were not attempted beyond $Re = 5600$ because for the glycerol mixture, the Froude number ($\Omega^2 R/g$, where g is gravity) is no longer small and the validity of a flat free-surface approximation becomes questionable. A sequence of flow visualisations covering the three main zones ($m = 3$, stability island, $m = 2$) is shown in figure 5 for $Re = 2100$, 3300 and 5545. In the first row, the photographs are taken a few revolutions after ink injection, but the number of peripheric vortices is already well identified. In the second row, the photographs are taken at a later time at which the ink patterns are only diffusing. At this later time, the ink ends up concentrated in the core of these vortices which, as a consequence, appear thinner in figure 5(d) and 5(f). This introduces a qualitative distinction between short and long observation times, related to the typical shearing timescale of the ink. Visualisations stemming from the nonlinear simulations of the new model have been included in the last row for the exact same values of Re . These visualisations will be discussed later.

We briefly comment on the robustness of these results with respect to experimental conditions, especially the age of the aqueous preparation. Two extreme situations can occur if the preparation is either too young or too old. If the measurements are performed on the same day as the preparation, the variability of the results is much higher and the modal selection is impacted in a way inconsistent with the tracing of a reproducible bifurcation diagram. Instead of the first unstable mode $m = 3$, LDV measurements as well as visualisations indicate the occurrence of modes $m = 2$ in water, or even $m = 4$ in glycerol mixtures (the latter with amplitudes barely higher than the noise level). The higher variability and the possible occurrence of an $m = 4$ mode were confirmed experimentally for lower glycerol contents of 20 % and 40 %. The dependence of the modal selection on the quality of water has been raised by Lopez *et al.* (2004). Indeed, if the preparation is left at rest in the laboratory for longer than a day, the modal selection favours the appearance of an $m = 3$ mode at onset, whatever the fluid. The protocol of waiting for 1 day to obtain a contaminated surface is consistent with that of Bernal *et al.* (1989). Fluid ageing also impacts the selection of the second unstable mode, especially the hysteresis: beyond 3–4 days, in glycerol experiments with descending Re (see Appendix C), a mode $m = 2$ has been identified to persist down to values of Re for which a stable base flow is expected. This mode $m = 2$ may even overlap completely with the stability island. This confirms that the instantaneous chemistry of the interface does influence crucial stability characteristics

such as the modal selection. The difficulties associated with the accurate tracking in time of the chemical composition reinforce the need for a simple model. In the remainder of this article, to avoid the complications associated with multistability, we only focus on the time window between 1 and 3 days where the experimental variability is minimal and the results are self-consistent.

4.2. Linear stability analysis

The linear stability analysis (LSA) of the base flow is the classical numerical way to predict the modal selection from the governing equations, at least in the presence of supercritical bifurcations. Assuming a perturbation to the base flow in the form $e^{\lambda t + im\theta}$, a mode is unstable if the real part $\text{Re}(\lambda)$ of the complex associated eigenvalue λ is strictly positive, else it is linearly stable. LSA parametrised by Re was performed for the two main models, respectively free-slip and the model with $U_r = 0$. $\text{Re}(\lambda)$ is shown versus Re in figures 6(a) and 6(b). Only the modes with $m = 2, 3$ and 4 were considered. For the free-slip model, the first unstable mode is the mode $m = 2$ above $Re = 3505$. No branch of $m = 3$ is unstable before $Re = 4755$. In contrast, for the new model, a branch of $m = 3$ modes destabilises somewhere between $Re = 1580$ and 2650 . The next instability involves a mode $m = 2$ from $Re = 3635$ on. All critical Reynolds numbers are given rounded by ± 5 , with an accuracy of a few percent (see Appendix B). They have been computed using a grid of 160×160 cells in r and z like in the nonlinear simulations. The curve $\text{Re}(\lambda) = f(Re)$ for the $m = 2$ mode appears in figures 6(a) and 6(b), common to the two models. However, the most unstable $m = 3$ branch seems specific to the new model and has no obvious stress-free counterpart. Additionally, the experimental selection mimics qualitatively the stability of the base flow for the new model, whereas the instabilities of the stress-free model are not consistent with the experimental observations. In particular, the stress-free model does not predict the first $m = 3$ instability and, as a consequence, misses the instability island altogether.

Eventually, the robustness of the bifurcation diagram in figure 6(b) was investigated by considering, instead of the base flow predicted by the exact model with $U_r = 0$, the base flow reconstructed from the fitted experimental profile at the interface (see § 3.3). Although the reconstructed velocity fields differ (see figure 4), their stability characteristics for $m = 2$ and 3 are very similar, as shown in figure 6(b). In particular, the modal selection $m = 3, 0$ and 2 obtained as Re increases is common to both new models whereas it is missed by the free-slip model.

4.3. Quantitative bifurcation diagrams

If the modal selection process can be well explained and predicted by linear theory, quantitative bifurcation diagrams demand nonlinear simulations. We demonstrate below that nonlinear simulations of the suggested model respect the modal selection predicted by LSA, but also match well the amplitude levels measured experimentally.

The main quantity measured experimentally using LDV is the pointwise axial velocity at a given location in the fixed laboratory frame. In such a frame, the saturation of a mode with both $\text{Im}(\lambda)$ and m non-zero leads in the simplest scenario to a rotating wave with angular phase velocity $\text{Im}(-\lambda)/m$. The amplitude of the associated time oscillations is characterised by the standard mean deviation of the measured velocity probe, denoted u_z^{rms} . This quantity is depicted in figure 7. Two different campaigns corresponding to two different fluids are reported: water as well as a water–glycerol mixture with 60 % glycerol in mass. The same quantity u_z^{rms} was measured in the nonlinear simulations

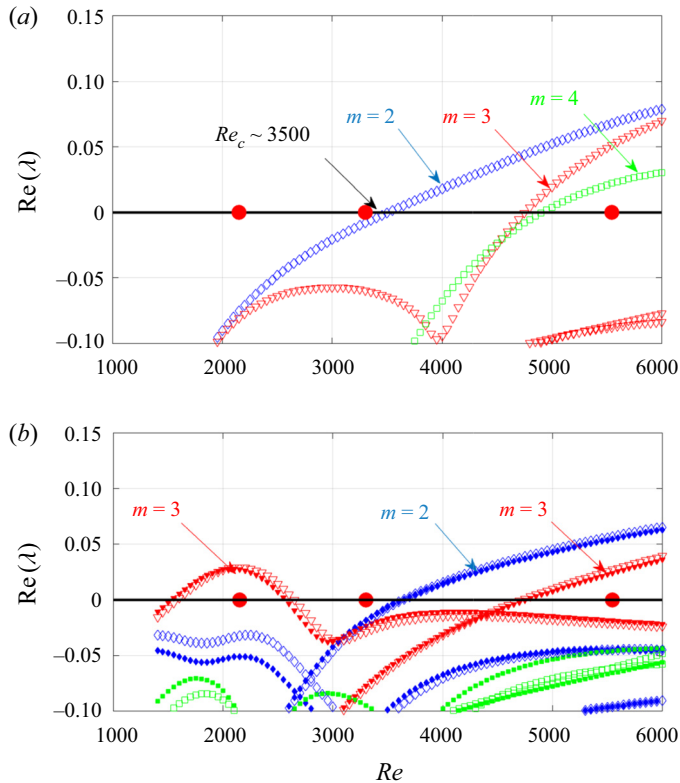


Figure 6. Growth rate $\text{Re}(\lambda)$ of the least damped eigenmodes versus Re (blue, $m = 2$; red, $m = 3$; green, $m = 4$). (a) Stress-free boundary condition; (b) new boundary condition (open symbols) and fitted boundary condition (closed symbols). The thick red dots correspond to the values of Re with visualisations in figure 5.

at essentially the same measurement station $(r, z) = (0.8, 0.125G)$. For both fluids and for values of Re around 3000, the experimental noise represents less than 0.5 % of the amplitude. Both experiments as well as the DNS display a clear bump in their bifurcation diagram corresponding to the occurrence of the saturated $m = 3$ mode. All three datasets predict a maximum amplitude of approximately 0.0097–0.012 located in the Re -interval 2000–2400. The maximum amplitude obtained for water occurs at the larger Reynolds number. Considering the differences between the experimental fluids and the crudeness of the model, this appears hence as a quantitatively decent comparison, especially when compared with the stress-free model which does not capture the instability with $m = 3$. The stability island is also well captured by the nonlinear simulations, although they tend to overpredict its width in the case of water.

The occurrence of the $m = 2$ instability is harder to quantify because of the presence of a hysteresis zone. The bounds of this hysteresis zone have been estimated experimentally by raising Re up to 5600, and decreasing Re from there in steps of 100 to 200. The DNS data confirms this hysteresis by revealing the existence of two different amplitude levels, the lower one with $u_z^{rms} \approx 5 \times 10^{-3}$ and the higher one with amplitudes closer to 3×10^{-2} . Such a distinction is not possible in the present experiment, because the level 5×10^{-3} appears comparable to the noise level. The details of the experimental and numerical protocols are given in Appendix C.

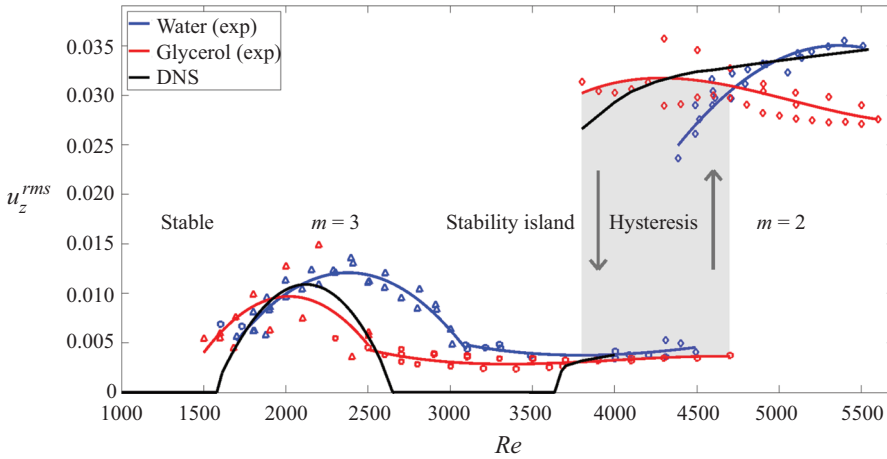


Figure 7. Amplitude bifurcation diagram. Temporal standard deviation u_z^{rms} versus Re . Experimental LDV measurements at location $(r, z) = (0.74 \pm 0.01, 0.5G)$ with water (blue dots) or 60 % glycerol–water mixture (red dots) versus DNS using the new model (black lines) at location $(r, z) = (0.8, 0.5G)$. The blue and red solid lines correspond to local second-order polynomial fits. A hysteresis area has been indicated symbolically in grey.

The angular phase velocities for the rotating wave, estimated from experiments, DNS and LSA, compare very well. In the experiments at $Re = 2100$ and $Re = 5545$, the modal structure (respectively $m = 3$ and $m = 2$) precesses in the prograde direction with a lag, as it propagates at angular velocity 0.65 (respectively 0.55). The corresponding values are 0.63 (respectively 0.54) in DNS and 0.64 (respectively 0.54) in LSA, which suggests that the angular phase velocity is weakly affected by nonlinearity. Further analysis of the spectrum at $Re = 5545$ shows that in addition to the dominant modes $m = 2$ and $m = 3$, only few harmonics are of significant energy level. These values also compare well with the angular velocity of 0.62 reported by Miraghaie *et al.* (2003) for $Re = 2000$. We are confident that the structures identified both experimentally and using the new model correspond to the same mode.

Furthermore, the location of the vortical structures can be compared between experiments and numerics by monitoring respectively the location where the ink (respectively a passive tracer) concentrates (figures 5d and 5f). In the rotating frame of the wave, the numerical velocity field at the interface is steady but not incompressible in the plane. The vortex centres in this plane stand here as stable fixed points for the Lagrangian motion of passive tracers. These points are located at a radius 0.62 for $Re = 2100$ and 0.65 for $Re = 5545$, whereas experiments with ink suggest the respective values of 0.64 and 0.68. These values are consistent with the location of the extrema of axial vorticity below the interface (see figures 5g and 5i). Despite a small shift in the radial position, the match is fair given the experimental uncertainty.

We define next the instantaneous flow rate $Q(t)$ through any meridian cross-section by

$$Q = \int_0^G \int_0^1 u_\theta \, dr \, dz. \tag{4.1}$$

In practice, we use a normalised form of Q , namely $Q^* = Q/Q_0$, where $Q_0 = \iint r \, dr \, dz$ is the flow rate corresponding to the equivalent solid body rotation flow with the same angular velocity. Because the present flow is entrained only by the rotating disc, less fluid

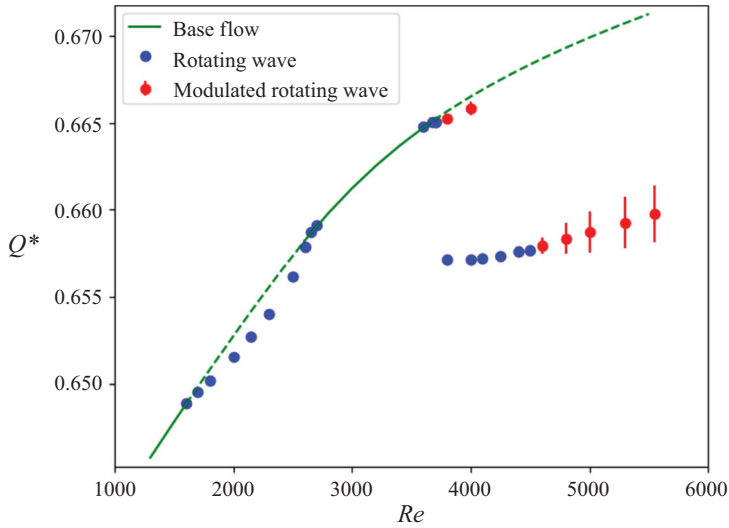


Figure 8. Normalised azimuthal flow rate Q^* versus Re (DNS). Stable steady axisymmetric base flow (solid green), unstable axisymmetric base flow (dashed green), rotating wave $m = 3$ or lower/upper branch $m = 2$ mode (blue dots) and time-modulated $m = 2$ mode (red dots). The vertical bars indicate the temporal fluctuations.

is entrained compared to solid-body rotation, and hence $0 < Q^* < 1$. Here, Q^* can not be estimated experimentally, but its estimates from DNS are reported in figure 8 versus Re . One advantage of the quantity Q^* over the variance of u_z is that rotating waves are associated with fixed points of Q^* rather than limit cycles, while unsteady time series of $Q^*(t)$ are the signature of temporally modulated rotating waves. Two supplementary modulational instabilities of the rotating wave with $m = 2$ have been identified in figure 8, one with very small modulational amplitude and another one (which we refer to as ‘lower branch’) with larger amplitudes, bifurcating from a new (disconnected) branch of rotating waves. The existence of several such branches is consistent with the hysteresis mentioned in the description of figure 7. Figure 9 contains an additional characterisation of the states found along the lower branch of figure 8, extracted from the times series of $Q^*(t)$. It contains notably the modulation amplitude A_{Q^*} versus Re , extracted from the min–max extrema and the main modulation frequency $f_0(Re)$ deduced from the frequency spectrum. The continuous growth of the amplitude versus Re in panel (a) and the almost constant frequency in panel (b) both support the emergence of this branch via a supercritical Neimark–Säcker bifurcation. Characteristics of the modulational states found along the lower branch, such as their amplitude and temporal frequency, are reported in figure 9. The onset of the modulation for $m = 2$ lies at $Re = Re_M^{(m=2)}$ between 4250 and 4400. The modulation amplitude increases apparently with Re but was not monitored beyond $Re = 5500$ (note that the snapshot displayed in figure 5(i) corresponds to a time prior to the development of the temporal modulation). The experimental measurements are not accurate enough to reveal whether this modulation is present or not, at least when Re is sufficiently low. Interestingly, preliminary nonlinear simulations of the stress-free model with similar resolution have indicated a similar modulational instability (Faugaret 2020). The modulation of the saturated mode $m = 2$ seems thus to be common to both models, although a deeper investigation of the limitations of the model would be necessary to conclude.

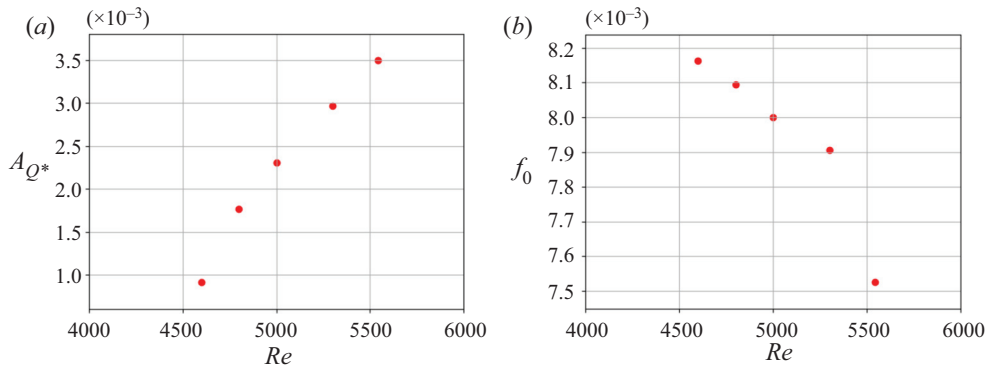


Figure 9. Characteristics of modulated states along the lower branch of figure 8 as a function of Re : (a) amplitude $A_{Q^*}(Re)$; (b) frequency $f_0(Re)$.

5. Conclusions

The present experimental and numerical study sheds light on the effect of arbitrary pollutants on the stability of a model swirling flow. This flow is generated by a rotating bottom lid and open at the top. It was originally selected because of previously ambiguous conclusions about the selection of the most unstable modes at least for small aspect ratios. The modal mismatch, as in Faugaret *et al.* (2020), is attributed to the small but unavoidable presence of pollutants on the free surface. Although small and poorly measurable in practice, these pollutants turn out to have a strong influence on the stability of the flow. Simulating the whole system of equations together with the transport of the pollutants (modelled as simple-species surfactants) should include the precise knowledge of the chemical composition of the interface, a Marangoni closure and many physical constants to be determined. We circumvent this complexity by assuming a parameter-free description both easily accessible and easy to implement in a numerical code. We suggest hence a Dirichlet boundary condition for the radial velocity field alone. The steady base flow and the perturbation are treated separately: the radial velocity is assumed to vanish for the base flow while for the perturbation, the usual stress-free conditions are retained. This paper explores the nonlinear dynamics of the flow for an aspect ratio of $G = 1/4$, as in Hirsá *et al.* (2001), both using an experimental set-up and an adapted DNS code with the aforementioned boundary condition. The stability thresholds for modes with different rotational symmetries are well reproduced by the model, where the stress-free boundary conditions fails quantitatively as well as qualitatively. The experimental bifurcation diagram, including as Re increases a saturated $m = 3$ mode followed by a stability island and the emergence of an $m = 2$ mode, are all well reproduced quantitatively by the nonlinear simulations. Both models predict a modulational instability of the $m = 2$ wave, a result yet to be verified experimentally. The different modal selections and the associated nonlinear dynamics result from subtle changes in the structure of the base flow. The instability of the $m = 3$ mode and the stability island are both absent in the more common stress-free model. This emphasizes the relevance of the new model. However, the applicability of this new model has also limitations revealed by the comparison with experiments. Aqueous solutions either too fresh (yet unaffected by the adsorption of pollution) or too old possess instability features not captured by the model. For a too young liquid mixture, the modal selection is no longer predicted by the model, with modes $m = 2$ and $m = 4$ replacing the mode $m = 3$ for the same parameters. For a too old

liquid mixture instead, the width of the hysteresis zone overlaps with the stability island and the bifurcation diagram of figure 7 becomes invalid. The experimental variability appears also less pronounced for tap water than for the water–glycerol mixtures. This suggests, for the present experimental water set-up, a need to select a specific temporal window from one to 3–4 days such that experimental variability is minimised. This result is experiment-dependent but has proven robust regardless of the exact water mixture considered. Future desirable developments of this modelling approach include non-flat interfaces when the Froude number increases (Kahouadji & Martin Witkowski 2014; Carrión *et al.* 2017; Tasaka & Iima 2017) and possible dewetting regimes (Jansson *et al.* 2006; Mougel *et al.* 2017; Yang *et al.* 2019, 2020; Rashkovan *et al.* 2021). Using a multiphase formalism, Yang *et al.* (2020) have shown that the motion in the gas phase above the interface is not relevant. However, the influence of denser fluids, as in the recent numerical simulations of Carrión *et al.* (2020), should be investigated. Two-dimensional particle image velocimetry, as used in the same flow set-up by Miraghaie *et al.* (2003) in horizontal planes or by Carrión *et al.* (2020) in meridian planes, could be a complementary way of analysing experiments. The approach developed in the present paper should also be generalised to non-axisymmetric geometries.

Acknowledgements. The authors thank the technical team CTEMO at LISN for their help with the experimental facility.

Funding. This work was supported by the French Agence Nationale de la Recherche under the ANR ETAE Project No. ANR-16-CE08-0011. HPC resources from GENCI-IDRIS (Grant No. 2017-2a10308) are also acknowledged.

Declaration of interest. The authors report no conflict of interest.

Author ORCIDs.

- Antoine Faugaret <https://orcid.org/0000-0001-6417-3005>;
- Yann Duguet <https://orcid.org/0000-0001-6258-0475>;
- Yann Fraigneau <https://orcid.org/0000-0001-9104-1569>;
- Laurent Martin Witkowski <https://orcid.org/0000-0003-0491-2384>.

Appendix A. Numerical methods for nonlinear simulations

We present in this appendix the main features of the numerical methods used in the code called Sunfluidh to solve the incompressible Navier–Stokes equations in 3-D cylindrical geometry. We first detail the time-marching procedure to estimate the velocity field at each time step (here, for simplicity Δt is assumed constant). We then present the projection method used to ensure a divergence-free velocity field. We conclude with the discrete operators involved in the Navier–Stokes equations in a 3-D cylindrical geometry.

A.1. Time-marching procedure

The time-marching procedure is based on the second-order backward differentiation formula. The viscous terms are treated implicitly to increase the numerical stability with respect to the timestep. We obtain the time-discrete system:

$$\frac{3\mathbf{u}^{n+1,*} - 4\mathbf{u}^n + \mathbf{u}^{n-1}}{2\Delta t} + \mathbf{F}_u^{n,n-1} = -\mathbf{G}_p^n + \mathbf{L}\mathbf{u}^{n+1}, \quad (\text{A1})$$

where the superscripts $n + 1$, n and $n - 1$ denote successive time steps, \mathbf{G}_p^n is the discrete pressure gradient at $n\Delta t$, $\mathbf{L}\mathbf{u}^{n+1}$ is the viscous term and $\mathbf{F}_u^{(n,n-1)}$ is the discrete convection

flux estimated at time $(n + 1)\Delta t$ from the linear extrapolation

$$F_u^{n,n-1} = 2F_u^n - F_u^{n-1}. \quad (\text{A2})$$

The system is rearranged in an incremental form

$$H_u \delta u = \left(\mathbb{1} - \frac{2\Delta t}{3} \cdot L \right) \delta u = S^{n,n-1} \cdot \frac{2\Delta t}{3}, \quad (\text{A3})$$

$\delta u = u^{n+1,*} - u^n$ and $S^{n,n-1}$ is the right-hand side term which gathers all explicit contributions from the time discretisation, the convection terms and the explicit contributions of the viscous terms. We specify each velocity component is solved separately what leads to the resolution of three independent systems $H_i \delta u_i = \frac{2}{3} \Delta t \cdot S_i^{n,n-1}$ with $i = r, \theta, z$.

As the spatial discretisation is carried out using a second-order centred scheme (see § A.3.2), H_i can be approximated by means of a factorisation procedure that leads to the resolution of three tridiagonal systems (one per direction). This technique is based on the work of Peaceman & Rachford (1955) that has been then adapted and largely used for different applications (see for instance Beam & Warming 1976; Kim & Moin 1985; Verzicco & Orlandi 1996). At the end of this step, the velocity field $u^{n+1,*}$ is not yet divergence-free.

A.2. Projection method

The divergence-free velocity field u^{n+1} is obtained by means of a projection method (Guermond, Mineev & Shen 2006) used in an incremental form proposed by Goda (1979). This consists in solving the Poisson equation

$$\nabla^2 \phi = \frac{\nabla \cdot u^{n+1,*}}{\Delta t}, \quad (\text{A4})$$

with zero normal derivative as boundary condition. The pressure and the velocity fields are thus updated between time n and $n + 1$ according to

$$p^{n+1} = p^n + \phi, \quad (\text{A5})$$

$$u^{n+1} = u^n - \frac{2\Delta t}{3} \nabla \phi - \frac{1}{Re} \nabla \cdot u^{n+1,*}. \quad (\text{A6})$$

The resolution of the Poisson equation is performed using a direct method based on a Fourier expansion along the azimuthal direction coupled with a partial diagonalisation technique. This method is based on the work of Haidvogel & Zang (1979) and has been used for instance by Barbosa & Daube (2005).

A.3. Spatial discretisation

A.3.1. Grid and coordinates

The Navier–Stokes equations are discretised on a staggered grid in cylindrical geometry. The indexation is defined as r_i, θ_j and z_k for the radial, azimuthal and axial coordinates, respectively. For each cell $C(i, j, k)$, the scalar quantities (i.e. the pressure P) are evaluated at the cell centre whereas the velocity components (u_r, u_θ, u_z) are evaluated at the centre of cell faces, see figure 10(a). For the cells adjacent to the axis, only the radial velocity component is evaluated at the axis (see figure 10(b)).

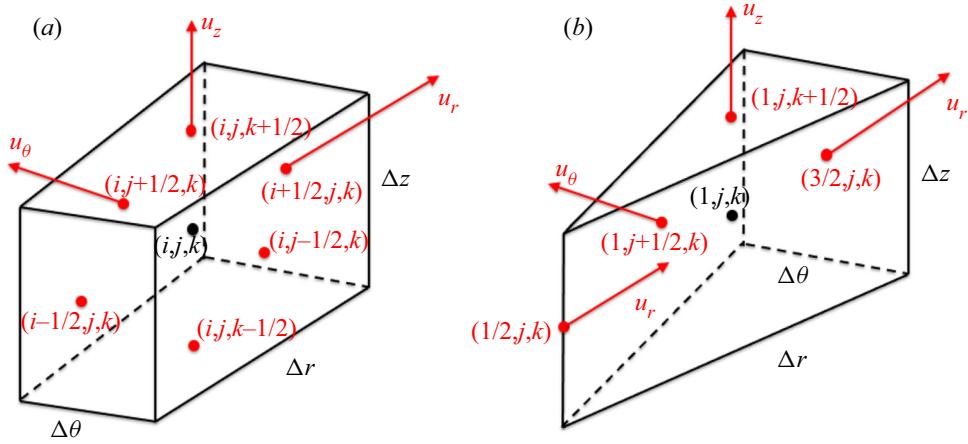


Figure 10. Coordinate location and positions of the physical quantities evaluated in the cells $C(i, j, k)$ (black tag, scalar quantities; red tags, velocity components). Cells away from the axis (a). Cells adjacent to the axis (b).

The relations between the radial coordinate sets are given by

$$r_i = \frac{1}{2}(r_{i+1/2} + r_{i-1/2}), \quad (\text{A7})$$

$$\Delta r_i = r_{i+1/2} - r_{i-1/2}, \quad (\text{A8})$$

$$\Delta r_{i+1/2} = r_{i+1} - r_i. \quad (\text{A9})$$

For the sake of simplicity, we suppose a regular distribution along the radius. We thus have $\Delta r_{i,j,k} = \Delta r_{i+1/2,j,k} = \Delta r$. The same convention is considered to define the azimuthal (θ) and axial (z) coordinates along the j and k directions, respectively.

A.3.2. Discrete operators

The operators applied to the pressure P and velocity components (u_r, u_θ, u_z) are discretised using a second-order centred scheme. For the sake of clarity, only the varying index is written down. We also define the space averaging operator in the l -direction for any quantity ϕ as

$$\bar{\phi}^l = \frac{1}{2}(\phi_{l+1} + \phi_l). \quad (\text{A10})$$

- The pressure gradient operator G_P :
 - in the u_r equation along the radial direction, $G_{i+1/2}(p) = (p_{i+1} - p_i)/\Delta r$;
 - in the u_θ equation along the azimuthal direction, $G_{j+1/2}(p) = (p_{j+1} - p_j)/(r_i \Delta \theta)$;
 - in the u_z equation along the axial direction, $G_{k+1/2}(p) = (p_{k+1} - p_k)/\Delta z$.
- The velocity divergence operator (in the source term of the Poisson equation):

$$\begin{aligned} \nabla \cdot \mathbf{u} &= \frac{1}{r_i \Delta r} (r_{i+1/2} u_{r,i+1/2} - r_{i-1/2} u_{r,i-1/2}) \\ &+ \frac{1}{r_i \Delta \theta} (u_{\theta,j+1/2} - u_{\theta,j-1/2}) \\ &+ \frac{1}{\Delta z} (u_{z,k+1/2} - u_{z,k-1/2}). \end{aligned} \quad (\text{A11})$$

A simple model for rotating free-surface flows

- The convective flux balance in a conservative form $F_u = \nabla \cdot (\mathbf{u} \otimes \mathbf{u})$:
 - for u_r at $(i + \frac{1}{2}, j, k)$,

$$\begin{aligned}
 F(u_r) = & \frac{1}{r_{i+1/2}\Delta r} (r_{i+1}\bar{u}_{r_{i+1}}^i \bar{u}_{r_{i+1}}^i - r_i \bar{u}_{r_i}^i \bar{u}_{r_i}^i) \\
 & + \frac{1}{r_{i+1/2}\Delta\theta} (\bar{u}_{r_{j+1/2}}^j \bar{u}_{\theta_{j+1/2}}^i - \bar{u}_{r_{j-1/2}}^j \bar{u}_{\theta_{j-1/2}}^i) \\
 & + \frac{1}{\Delta z} (\bar{u}_{r_{k+1/2}}^k \bar{u}_{z_{k+1/2}}^i - \bar{u}_{r_{k-1/2}}^k \bar{u}_{z_{k-1/2}}^i) \\
 & - \frac{u_{r,i+1/2,j,k}^2}{r_{i+1/2}}; \tag{A12}
 \end{aligned}$$

- for u_θ at $(i, j + \frac{1}{2}, k)$,

$$\begin{aligned}
 F(u_\theta) = & \frac{1}{r_i\Delta r} (r_{i+1/2}\bar{u}_{\theta_{i+1/2}}^i \bar{u}_{r_{i+1/2}}^j - r_{i-1/2}\bar{u}_{\theta_{i-1/2}}^i \bar{u}_{r_{i-1/2}}^j) \\
 & + \frac{1}{r_i\Delta\theta} (\bar{u}_{\theta_{j+1}}^j \bar{u}_{\theta_{j+1}}^j - \bar{u}_{\theta_j}^j \bar{u}_{\theta_j}^j) \\
 & + \frac{1}{\Delta z} (\bar{u}_{\theta_{k+1/2}}^k \bar{u}_{z_{k+1/2}}^j - \bar{u}_{\theta_{k-1/2}}^k \bar{u}_{z_{k-1/2}}^j) \\
 & + \frac{\frac{1}{2}(\bar{u}_{r_{i+1/2}}^j + \bar{u}_{r_{i-1/2}}^j)u_{\theta,i,j+1/2,k}}{r_i}; \tag{A13}
 \end{aligned}$$

- for u_z at $(i, j, k + \frac{1}{2})$,

$$\begin{aligned}
 F(u_z) = & \frac{1}{r_i\Delta r} (r_{i+1/2}\bar{u}_{z_{i+1/2}}^i \bar{u}_{r_{i+1/2}}^k - r_{i-1/2}\bar{u}_{z_{i-1/2}}^i \bar{u}_{r_{i-1/2}}^k) \\
 & + \frac{1}{r_i\Delta\theta} (\bar{u}_{z_{j+1/2}}^j \bar{u}_{\theta_{j+1/2}}^k - \bar{u}_{z_{j-1/2}}^j \bar{u}_{\theta_{j-1/2}}^k) \\
 & + \frac{1}{\Delta z} (\bar{u}_{z_{k+1}}^k \bar{u}_{z_{k+1}}^k - \bar{u}_{z_k}^k \bar{u}_{z_k}^k). \tag{A14}
 \end{aligned}$$

- The viscous terms (Laplacian operator):
 - for u_r at $(i + \frac{1}{2}, j, k)$,

$$\begin{aligned}
 L(u_r) = & \frac{1}{r_{i+1/2}\Delta r} (r_{i+1} \frac{u_{r,i+3/2} - u_{r,i+1/2}}{\Delta r} - r_i \frac{u_{r,i+1/2} - u_{r,i-1/2}}{\Delta r}) \\
 & + \frac{1}{r_{i+1/2}^2\Delta\theta} \left(\frac{u_{r,j+1} - u_{r,j}}{\Delta\theta} - \frac{u_{r,j} - u_{r,j-1}}{\Delta\theta} \right)
 \end{aligned}$$

$$\begin{aligned}
 & + \frac{1}{\Delta z} \left(\frac{u_{r,k+1} - u_{r,k}}{\Delta z} - \frac{u_{r,k} - u_{r,k-1}}{\Delta z} \right) \\
 & - \frac{2}{r_{i+1/2}^2} \left(\frac{\bar{u}_{\theta j+1/2}^i - \bar{u}_{\theta j-1/2}^i}{\Delta \theta} \right) \\
 & - \frac{u_{r,i+1/2,j,k}}{r_{i+1/2}^2};
 \end{aligned} \tag{A15}$$

- for u_θ at $(i, j + \frac{1}{2}, k)$,

$$\begin{aligned}
 L(u_\theta) & = \frac{1}{r_i \Delta r} \left(r_{i+1/2} \frac{u_{\theta,i+1} - u_{\theta,i}}{\Delta r} - r_{i-1/2} \frac{u_{\theta,i} - u_{\theta,i-1}}{\Delta r} \right) \\
 & + \frac{1}{r_i^2 \Delta \theta} \left(\frac{u_{\theta,j+3/2} - u_{\theta,j+1/2}}{\Delta \theta} - \frac{u_{\theta,j+1/2} - u_{\theta,j-1/2}}{\Delta \theta} \right) \\
 & + \frac{1}{\Delta z} \left(\frac{u_{\theta,k+1} - u_{\theta,k}}{\Delta z} - \frac{u_{\theta,k} - u_{\theta,k-1}}{\Delta z} \right) \\
 & + \frac{2}{r_i^2} \left(\frac{\bar{u}_{rj+1}^i - \bar{u}_{rj}^i}{\Delta \theta} \right) \\
 & - \frac{u_{\theta,i,j+\frac{1}{2},k}}{r_i^2};
 \end{aligned} \tag{A16}$$

- for u_z at $(i, j, k + \frac{1}{2})$,

$$\begin{aligned}
 L(u_z) & = \frac{1}{r_i} \left(\frac{1}{\Delta r} \left(r_{i+1/2} \frac{u_{z,i+1} - u_{z,i}}{\Delta r} - r_{i-1/2} \frac{u_{z,i} - u_{z,i-1}}{\Delta r} \right) \right) \\
 & + \frac{1}{r_i^2 \Delta \theta} \left(\frac{u_{z,j+1} - u_{r,j}}{\Delta \theta} - \frac{u_{z,j} - u_{z,j-1}}{\Delta \theta} \right) \\
 & + \frac{1}{\Delta z} \left(\frac{u_{z,k+3/2} - u_{z,k+1/2}}{\Delta z} - \frac{u_{z,k+1/2} - u_{z,k-1/2}}{\Delta z} \right).
 \end{aligned} \tag{A17}$$

A.4. Estimation of the radial velocity at the axis

Consistently with the numerical scheme detailed above, we need to estimate the radial velocity component u_r at the axis (see [figure 10b](#)). We rely on results from Lewis & Bellan (1990), where non-zero values of u_r and u_θ at the axis are only related to the first (complex) azimuthal Fourier mode $(\widehat{u}_r^{(1)}, \widehat{u}_\theta^{(1)})$, for any z plane. They showed that

$$\widehat{u}_r^{(1)} = -i \cdot \widehat{u}_\theta^{(1)} \quad (\text{with } i^2 = -1), \tag{A18}$$

with

$$\widehat{u}_\theta^{(1)} = \lim_{r \rightarrow 0} \frac{1}{2\pi} \int_0^{2\pi} u_\theta(r, \theta) e^{-i\theta} d\theta. \tag{A19}$$

Thanks to (A18) and (A19), we can estimate the values of u_r at the axis as a function of θ , for any z plane,

$$u_r(0, \theta) = \widehat{u}_r^{(1)} e^{-i\theta} = u_x^0 \cos \theta + u_y^0 \sin \theta, \tag{A20}$$

linked to the Cartesian velocity components u_x^0 and u_y^0 . The latter are easily evaluated as

$$u_x^0 = \lim_{r \rightarrow 0} -\frac{1}{2\pi} \int_0^{2\pi} u_\theta(r, \theta) \sin \theta \, d\theta \approx -\frac{1}{2\pi} \sum_j \tilde{u}_{\theta_{j+1/2}} \cdot \sin \theta_{j+1/2} \cdot \Delta\theta, \quad (\text{A21})$$

$$u_y^0 = \lim_{r \rightarrow 0} \frac{1}{2\pi} \int_0^{2\pi} u_\theta(r, \theta) \cos \theta \, d\theta \approx \frac{1}{2\pi} \sum_j \tilde{u}_{\theta_{j+1/2}} \cdot \cos \theta_{j+1/2} \cdot \Delta\theta, \quad (\text{A22})$$

where $\tilde{u}_{\theta_{j+1/2}}$ is an extrapolation of u_θ to the axis along the radial direction.

Appendix B. Numerical methods for the linear stability analysis (LSA)

The numerical linear stability analysis is a two-step process. The first step consists in computing the nonlinear steady axisymmetric base flow for a given Reynolds number. The second step consists in finding the eigenmodes (eigenvalues and eigenvectors) associated with the Navier–Stokes equations linearised around the base flow for a given azimuthal mode m . In our approach, we solve all the equations coupled as a large-size sparse linear system arising from the spatial discretisation. The choice of an efficient linear solver for non-Hermitian matrices is crucial for good performances.

B.1. Base flow computations

In the radial and axial directions, we have used the same spatial discretisation as for the nonlinear code Sunfluidh (cf. Appendix A). There is no temporal discretisation as only steady-state solutions are sought. Instead of solving a Poisson equation for the pressure, the divergence-free velocity field is obtained by solving the genuine velocity divergence operator on pressure grid nodes. This equation is coupled with the momentum equations. To avoid indeterminacy, a reference value for the pressure is imposed at an arbitrary grid point. The large algebraic nonlinear system of equations is solved using a Newton–Raphson algorithm. In the present configuration, five iterations are typically enough to obtain convergence to machine precision when starting from a well-chosen initial guess. This guess is either a zero velocity field if Re is small enough (typically $Re = 500$) or a solution already computed for a near Reynolds number value. For each Newton–Raphson iteration, the algebraic system is solved owing to a direct sparse solver provided by common scientific packages, like Pardiso (Bollhöfer *et al.* 2020) or Umfpack (Davis 2004).

To validate the axisymmetric base flow, we also ran the three-dimensional Sunfluidh code at values of Re for which the flow is stable. At steady state and using the same grid in the meridional plane, both velocity fields match within 10^{-7} . An alternate formulation, namely a vorticity-stream function, (in fact a third code detailed by Kahouadji, Houchens & Martin Witkowski 2011) has been used for cross-checking purposes. In this latter comparison, the same results are obtained below 1%, which is consistent with the second-order finite difference discretisation used for both approaches.

B.2. Linear stability analysis

Once the base flow is obtained, the linearised Navier–Stokes equations together with the boundary conditions yield a generalised eigenvalue problem. To compute simultaneously a few selected eigenvalues, we use the implicit restarted Arnoldi method implemented in the Arpack library (Lehoucq, Sorensen & Yang 1998). We focus on the eigenvalues that

| Grid size | $Re_c^{(m=3)}$ | $Re_c^{(m=0)}$ | $Re_c^{(m=2)}$ |
|------------------|----------------|----------------|----------------|
| 160×160 | 1582.46 | 2648.76 | 3636.83 |
| 320×320 | 1583.63 | 2640.25 | 3626.00 |
| 640×640 | 1583.92 | 2638.17 | 3623.34 |

Table 1. Critical Reynolds number values Re_c : $Re_c^{(m=3)}$ for the transition from mode 0 to 3, $Re_c^{(m=0)}$ from 3 to 0 and $Re_c^{(m=2)}$ from 0 to 2 for three different grid resolutions. The cell size is halved every time the number of cells is doubled.

have the largest real part by selecting the shift-and-invert strategy in Arpack. In addition to the tolerance on the computed eigenvalues, set to machine accuracy, other choices must be prescribed: the shift value, the number of eigenvalues sought around the shift and the maximal dimension of the Krylov subspace. The shift value is chosen along the imaginary axis and should ideally be close to the imaginary part of the most unstable eigenmode. Experimental observations are a useful guide, we chose $-0.6m$ where m is the azimuthal mode. Forty eigenvalues are computed for a Krylov subspace dimension of 100. The most unstable eigenvalue can be overlooked if inappropriate choices are made for the shift and the number of eigenvalues. However, in addition to experimental evidence, *a posteriori* checks with the nonlinear code Sunfluidh show consistency between all approaches, as detailed below.

B.3. Validations

The adequacy of the 160×160 grid in (r, z) was checked in a spatial resolution convergence study for the three Reynolds numbers where there is a transition from (or to) an axisymmetric base flow in [figure 6\(b\)](#). The critical values Re_c of the Reynolds number are given in [table 1](#) for the new model (open symbols).

The results obtained using LSA shows variations of Re_c of less than 1 % as the grid size varies. This yields an estimate on the relative error for Re_c in numerical simulations. We can also be confident that a 160×160 grid resolution in the meridional plane for Sunfluidh is a good compromise between accuracy and computational cost.

Further validation is given by comparing the value of Re_c obtained by LSA and Sunfluidh using the following technique. With Sunfluidh, once the axisymmetric steady state is reached with machine accuracy in a stable region, a perturbation is applied to the velocity field with random noise, with an amplitude of 1 % of the maximum velocity. As seen in [figure 6\(b\)](#), the real parts of the eigenvalues are well separated, so that there is eventually a clear oscillatory exponential decay of the least unstable mode. Two decay rates have been estimated in the stability island for $Re = 2700$ and $Re = 2800$, with a fit in a logarithmic scale on the temporal series of any probe. Linear extrapolation of the two decay rates yields $Re_c = 2652.55$ with $\Delta t = 4 \times 10^{-3}$ and using the same meridional grid resolution as in LSA. This value compares favourably with the value 2648.76 in [table 1](#). The spatial structure of the mode $m = 3$ is also recovered when subtracting the base flow. This last test validates the choice of the azimuthal mode and of the shift for the LSA.

Appendix C. Experimental/numerical protocol for the investigation of hysteresis

In this section, we detail the exact protocol followed in parameter space to highlight hysteresis as a function of Re . In addition to the threshold detection experiments detailed

in § 2.1, several other experiments were performed to estimate the bounds of the hysteresis zone. These experiments consist in starting from $Re = 5600$, with a fully established mode $m = 2$, and then to decrease the Reynolds number in steps of 100 or 200. With the 60 % glycerol mixture, the Reynolds number was dropped to 2500. The decay of the mode $m = 2$ was observed for Re in [3800 : 4200]. The number of disc rotations at these steps was at least 80. With water, the return from the mode $m = 2$ to the axisymmetric case was observed for Re in [4300 : 4400]. Because of the lower kinematic viscosity of water and despite a two-to-four times longer time span per step compared with the glycerol experiments, the minimum number of disc rotations was only 45 for these values of Re . Yet, even with a number of disc rotations almost divided by two, transition happened at higher Re for water.

Hysteresis is also verified numerically for the same range of values of Re . A first set of DNSs was initialised by a zero velocity field for different values of Re in [4400 : 5545], and a second set by decreasing Re from 4500 to 3600. Each new case had started from the last temporal solution calculated at the previous Re . Similarly, a third set was carried out by increasing Re from 3600 to 4100. For each set, the steps in Re were fixed to values between 100 and 200. In each case, the observation time considered was chosen at least 1000 time units after reaching the established flow state.

REFERENCES

- BANDI, M.M., AKELLA, V.S., SINGH, D.K., SINGH, R.S. & MANDRE, S. 2017 Hydrodynamic signatures of stationary Marangoni-driven surfactant transport. *Phys. Rev. Lett.* **119**, 264501.
- BARBOSA, E. & DAUBE, O. 2005 A finite difference method for 3D incompressible flows in cylindrical coordinates. *Comput. Fluids* **34** (2), 950–971.
- BATCHELOR, G.K. 2000 *An Introduction to Fluid Dynamics*. Cambridge University Press.
- BEAM, R.M. & WARMING, R.F. 1976 An implicit finite-difference algorithm for hyperbolic systems in conservation-law form. *J. Comput. Phys.* **22**, 87–110.
- BERNAL, L.P., HIRSA, A., KWON, J.T. & WILLMARTH, W.W. 1989 On the interaction of vortex rings and pairs with a free surface for varying amounts of surface active agent. *Phys. Fluids* **1** (12), 2001–2004.
- BOLLHÖFER, M., SCHENK, O., JANALIK, R., HAMM, S. & GULLAPALLI, K. 2020 *State-of-the-Art Sparse Direct Solvers*, pp. 3–33. Springer International Publishing.
- BOUFFANAIS, R. & LO JACONO, D. 2009 Transitional cylindrical swirling flow in presence of a flat free surface. *Comput. Fluids* **38**, 1651–1673.
- CARRIÓN, L., HERRADA, M.A., SHTERN, V.N. & LÓPEZ-HERRERA, J.M. 2017 Patterns and stability of a whirlpool flow. *Fluid Dyn. Res.* **49** (2), 025519.
- CARRIÓN, L., NAUMOV, I.V., SHARIFULLIN, B.R., HERRADA, M.A. & SHTERN, V.N. 2020 Formation of dual vortex breakdown in a two-fluid confined flow. *Phys. Fluids* **32** (10), 104107.
- CHENG, N.S. 2008 Formula for the viscosity of a glycerol-water mixture. *Ind. Engng Chem. Res.* **47** (9), 3285–3288.
- COGAN, S.J., RYAN, K. & SHEARD, G.J. 2011 Symmetry breaking and instability mechanisms in medium depth torsionally open cylinder flows. *J. Fluid Mech.* **672**, 521–544.
- DAVIS, T.A. 2004 Algorithm 832: UMFPACK v4.3—an unsymmetric-pattern multifrontal method. *ACM Trans. Math. Softw.* **30** (2), 196–199.
- FAUGARET, A. 2020 Influence of air-water interface condition on rotating flow stability: experimental and numerical exploration. PhD thesis, Sorbonne Université, Paris, France.
- FAUGARET, A., DUGUET, Y., FRAIGNEAU, Y. & MARTIN WITKOWSKI, L. 2020 Influence of interface pollution on the linear stability of a rotating fluid. *J. Fluid Mech.* **900**, A42.
- GODA, K. 1979 A multistep technique with implicit difference schemes for calculating two- or three-dimensional cavity flows. *J. Comput. Phys.* **30**, 76–95.
- GUERMOND, J.L., MINEV, P.D. & SHEN, J. 2006 An overview of projection methods for incompressible flows. *Comput. Meth. Appl. Mech. Engng* **195**, 6011–6045.
- HAIDVOGEL, D.B. & ZANG, T. 1979 The accurate solution of Poisson's equation by expansions in Chebyshev polynomials. *J. Comput. Phys.* **30**, 167–180.

- HIRSA, A.H. & LOPEZ, J.M. 2021 Coupling vortical bulk flows to the air–water interface: from putting oil on troubled waters to surfactants on protein solutions. *Fluids* **6** (6), 198.
- HIRSA, A.H., LOPEZ, J.M. & MIRAGHAIE, R. 2001 Measurement and computation of hydrodynamic coupling at an air/water interface with an insoluble monolayer. *J. Fluid Mech.* **443**, 271–292.
- HUISMAN, S.G., VAN GILS, D.P.M. & SUN, C. 2012 Applying laser Doppler anemometry inside a Taylor–Couette geometry using a ray-tracer to correct for curvature effects. *Eur. J. Mech. (B/Fluids)* **36**, 115–119.
- HYUN, J.M. 1985 Flow in an open tank with a free surface driven by the spinning bottom. *Trans. ASME J. Fluids Engng* **107** (4), 495–499.
- IWATSU, R. 2004 Analysis of flows in a cylindrical container with rotating bottom and top underformable free surface. *JSME Intl J.* **47** (3), 549–556.
- IWATSU, R. 2005 Numerical study of flows in a cylindrical container with rotating bottom and top flat free surface. *J. Phys. Soc. Japan* **74** (1), 333–344.
- JANSSON, T.R.N., HASPANG, M.P., JENSEN, K.H., HERSEN, P. & BOHR, T. 2006 Polygons on a rotating fluid surface. *Phys. Rev. Lett.* **96**, 174502.
- KAHOUADJI, L. 2011 Analyse de stabilité linéaire d'écoulements tournants en présence de surface libre. PhD thesis, Université Pierre et Marie Curie, Paris, France.
- KAHOUADJI, L., HOUCHEMS, B.C. & MARTIN WITKOWSKI, L. 2011 Thermocapillary instabilities in a laterally heated liquid bridge with end wall rotation. *Phys. Fluids* **23**, 104104.
- KAHOUADJI, L. & MARTIN WITKOWSKI, L. 2014 Free surface due to a flow driven by a rotating disk inside a vertical cylindrical tank: axisymmetric configuration. *Phys. Fluids* **26**, 072105.
- KAHOUADJI, L., MARTIN WITKOWSKI, L. & LE QUÉRÉ, P. 2010 Seuil de stabilité pour un écoulement à surface libre engendré dans une cavité cylindrique tournante à petit rapport de forme. *Méc. Indust.* **11** (5), 339–344.
- KIM, J. & MOIN, P. 1985 Application of a fractional-step method to incompressible Navier–Stokes equations. *J. Comput. Phys.* **59**, 308–323.
- KWAN, Y.Y., PARK, J. & SHEN, J. 2010 A mathematical and numerical study of incompressible flows with a surfactant monolayer. *Discr. Contin. Dyn. Syst.* **28**, 181–197.
- LEHOUCQ, R., SORENSEN, D. & YANG, C. 1998 ARPACK users' guide - solution of large-scale eigenvalue problems with implicitly restarted Arnoldi methods. In *SIAM*.
- LEWIS, H.R. & BELLAN, P.M. 1990 Physical constraints on the coefficients of Fourier expansions in cylindrical coordinates. *J. Math. Phys.* **31**, 2592–2596.
- LOPEZ, J.M. 1995 Unsteady swirling flow in an enclosed cylinder with reflectional symmetry. *Phys. Fluids* **7**, 2700–2714.
- LOPEZ, J.M. & CHEN, J. 1998 Coupling between a viscoelastic gas/liquid interface and swirling vortex flow. *J. Fluids Engng* **120**, 655–661.
- LOPEZ, J.M. & HIRSA, A. 1998 Direct determination of the dependence of the surface shear and dilatational viscosities on the thermodynamic state of the interface: theoretical foundations. *J. Colloid Interface Sci.* **206** (1), 231–239.
- LOPEZ, J.M., MARQUES, F., HIRSA, A.H. & MIRAGHAIE, R. 2004 Symmetry breaking in free-surface cylinder flows. *J. Fluid Mech.* **502**, 99–126.
- MAGNAUDET, J. & EAMES, I. 2000 The motion of high-Reynolds-number bubbles in inhomogeneous flows. *Ann. Rev. Fluid Mech.* **32** (1), 659–708.
- MARTÍN, E. & VEGA, J.M. 2006 The effect of surface contamination on the drift instability of standing Faraday waves. *J. Fluid Mech.* **546**, 203–225.
- MIRAGHAIE, R., LOPEZ, J.M. & HIRSA, A.H. 2003 Flow induced patterning at the air–water interface. *Phys. Fluids* **15** (6), L45–L48.
- MOUGEL, J., FABRE, D., LACAZE, L. & BOHR, T. 2017 On the instabilities of a potential vortex with a free surface. *J. Fluid Mech.* **824**, 230–264.
- PEACEMAN, D.W. & RACHFORD, H.H. 1955 The numerical solution of parabolic and elliptic differential equations. *J. Soc. Ind. Appl. Maths* **3**, 28–41.
- PIVA, M. & MEIBURG, E. 2005 Steady axisymmetric flow in an open cylindrical container with a partially rotating bottom wall. *Phys. Fluids* **17** (6), 063603(12).
- PONCE-TORRES, A. & VEGA, E.J. 2016 The effects of ambient impurities on the surface tension. *EPJ Web Conf.* **114**, 02098.
- PONCET, S. & CHAUVE, M.P. 2007 Shear-layer instability in a rotating system. *J. Flow Visual. Image Process.* **14** (1), 85–105.
- RASHKOVAN, A., AMAR, S.D., BIEDER, U. & ZISKIND, G. 2021 Analysis of polygonal vortex flows in a cylinder with a rotating bottom. *Appl. Sci.* **11** (3), 1348.

A simple model for rotating free-surface flows

- SCRIVEN, L.E. 1960 Dynamics of a fluid interface: equation of motion for Newtonian surface fluids. *Chem. Engng Sci.* **12** (2), 98–108.
- SERRE, E. & BONToux, P. 2007 Vortex breakdown in a cylinder with a rotating bottom and a flat stress-free surface. *Intl J. Heat Fluid Flow* **28**, 229–248.
- SPOHN, A. & DAUBE, O. 1991 Recirculating flows in a cylindrical tank. In *V International Conference on Computational Methods and Experimental Measurement* (ed. A. Sousa, C.A. Brebbia & G.M. Carlomagno), pp. 155–166. Elsevier.
- SPOHN, A., MORY, M. & HOPFINGER, E.J. 1993 Observations of vortex breakdown in an open cylindrical container with a rotating bottom. *Exp. Fluids* **14**, 70–77.
- STONE, H. 1990 A simple derivation of the time-dependent convective-diffusion equation for surfactant transport along a deforming surface. *Phys. Fluids* **2**, 111–112.
- TASAKA, Y. & IIMA, M. 2017 Surface switching statistics of rotating fluid: disk-rim gap effects. *Phys. Rev. E* **95**, 043113.
- VERZICCO, R. & ORLANDI, P. 1996 A finite-difference scheme for three-dimensional incompressible flows in cylindrical coordinates. *J. Comput. Phys.* **123**, 402–414.
- VOGEL, M.J., MIRAGHAIE, R., LOPEZ, J.M. & HIRSA, A.H. 2004 Flow-induced patterning of Langmuir monolayers. *Langmuir* **20**, 5651–654.
- YANG, W., DELBENDE, I., FRAIGNEAU, Y. & MARTIN WITKOWSKI, L. 2019 Axisymmetric rotating flow with free surface in a cylindrical tank. *J. Fluid Mech.* **861**, 796–814.
- YANG, W., DELBENDE, I., FRAIGNEAU, Y. & MARTIN WITKOWSKI, L. 2020 Large axisymmetric surface deformation and dewetting in the flow above a rotating disk in a cylindrical tank: spin-up and permanent regimes. *Phys. Rev. Fluids* **5** (4), 044801.